Research Article Vol. 29, No. 10 / 10 May 2021 / Optics Express 14476

Optics EXPRESS

Silicon nitride polarization beam splitter based on polarization-independent MMIs and apodized Bragg gratings

JIAHAO ZHAN,[1] JOSEPH BROCK,[1] SYLVAIN VEILLEUX,[2] AND MARIO DAGENAIS[1,*]

[1] *Department of Electrical and Computer Engineering, University of Maryland, College Park, MD 20742, USA*
[2] *Department of Astronomy, University of Maryland, College Park, MD 20742, USA*
[*] *dage@umd.edu*

Abstract: We present the design and experimental results of a novel polarization beam splitter (PBS) with a high polarization extinction ratio (PER) made on a Si_3N_4 platform. The PBS is composed of two identical polarization-independent multi-mode interferometers and two identical apodized Bragg gratings. The operating principle of this device is based on the fact that the TE and TM stopbands of the grating are centered at different wavelengths. The reflected and transmitted light from the gratings are routed to separate output ports by the two-MMI configuration. The experimental results show that a PER of > 30 dB is achieved over a bandwidth of 22 nm, with an insertion loss of ~ 1.1 dB. The total length of the device is ~ 820 µm.

1. Introduction

On-chip polarization control is of great importance in integrated photonics. Since most waveguides exhibit different effective indices for TE and TM polarizations, on-chip photonic devices are typically designed for only one polarization. Therefore, it is often desired to have a polarization beam splitter (PBS) to separate TE and TM polarizations and handle them separately, which is the most important application of a PBS. For example, astrophotonics, which is an emerging field describing the application of integrated photonic technologies to astronomical sciences, is considered to be one promising avenue that will miniaturize the next-generation astronomical instrumentation [1]. Currently, a wide variety of on-chip astrophotonic devices are being developed, some of which have already demonstrated competitive performances [2–4]. As light collected by telescopes from celestial objects is unpolarized, astronomers are interested in the development of polarization-independent photonic devices, capturing all the light from faint celestial objects. In photonic quantum information systems, a PBS is an essential element for the generation and detection of polarization-entangled photon pairs [5,6]. As silicon photonics is considered to be a highly competitive route to quantum computing [7] and quantum communication [8], on-chip PBSs are expected to be widely applied in integrated quantum photonic systems in the near future.

Various approaches for high-performance PBSs have been proposed and implemented on both SOI and Si_3N_4 platforms, with structures based on directional couplers (DCs) [9–13], slot waveguides [11,14], sub-wavelength gratings (SWGs) [15], multi-mode interferometers (MMIs) [16–19] and Mach-Zehnder interferometers (MZIs) [20,21]. SOI-based PBSs typically feature a larger polarization extinction ratio (PER) within a smaller footprint, compared to their Si_3N_4 counterparts. One of the state-of-the-art SOI-based PBSs has a PER of > 30 dB over a 70 nm bandwidth [10], the other has a PER approaching 40 dB around the central wavelength [12]. Meanwhile, one of the devices on Si_3N_4 platforms has realized an PER of > 20 dB over a 38 nm

#420499
Journal © 2021

https://doi.org/10.1364/OE.420499
Received 25 Jan 2021; revised 9 Apr 2021; accepted 15 Apr 2021; published 28 Apr 2021

bandwidth (37 dB at central wavelength) [21], the other has achieved a very large bandwidth of > 100 nm with a PER of > 18 dB [19].

In this paper, a novel PBS with a high PER on a 300-nm thick Si_3N_4 platform is proposed, fabricated and experimentally characterized. This PBS consists of two polarization-independent MMIs (PI-MMIs) with two apodized Bragg gratings (ABGs). Experimental results show that a PER of > 30 dB is achieved over a bandwidth of ~ 22 nm, with an insertion loss (IL) ~ 1.1 dB.

The rest of the paper is organized as follows: Section 2 briefly discusses the design and operating principle of the device. Section 3 presents the methods for fabrication and characterization, together with the measurement results of a fabricated device. A comparison with other Si_3N_4-based PBSs and a brief discussion are given in Section 4, and the main conclusions are summarized in Section 5.

2. Principle of operation and device design

Depicted in Fig. 1 is a schematic drawing of the proposed PBS. Its operating principle relies on the fact that the TE and TM stopbands of a Bragg grating are centered at different wavelengths, and typically do not overlap. A 2×2 PI-MMI divides the input light from the upper input port equally into two output ports, with the lower one having a $\pi/2$ phase difference compared to the upper one, regardless of the input polarization. Similarly, if two light beams with a $\pi/2$ phase difference are injected into the two input ports of a 2×2 PI-MMI, they will be combined into the lower output port.

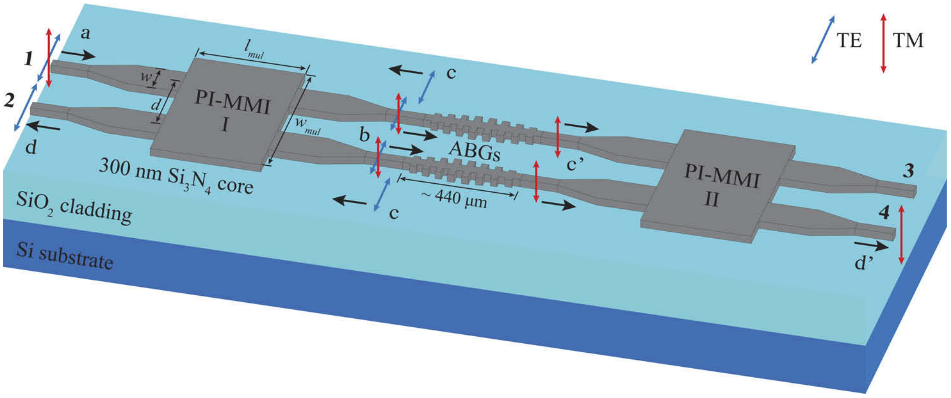

Fig. 1. Schematic of the proposed PBS, comprising two identical PI-MMIs and two ABGs. Letters associated with black arrows indicate light propagation inside the device. The SiO_2 top cladding is omitted in the drawing for a clear illustration.

As shown in Fig. 1, light with both polarizations at λ_0 is incident from port 1 into the first PI-MMI and split equally into cross and bar ports. Assume that the TE stopbands of the ABG is centered at λ_0, then the TE components will be reflected back into the first PI-MMI and combined into port 2, whereas the TM components will be transmitted, incident into the second PI-MMI and combined into port 4. Therefore, the two polarizations are separated.

2.1. *Design of the PI-MMI*

As discussed above, the two PI-MMIs in Fig. 1 act as routers to guide the reflected and transmitted light into different ports. Each PI-MMI is simply a 50:50 power splitter working for both TE and TM polarizations, which is able to split the input light evenly into the two output ports with a

$\pi/2$ phase difference. The beat length of an MMI is, as given in Ref. [22]:

$$L_{\pi,p} = \frac{\pi}{\beta_{0,p} - \beta_{1,p}} = \frac{\lambda}{2(n_{0,p} - n_{1,p})} \tag{1}$$

where λ is the operating wavelength, β_0, n_0 and β_1, n_1 are the propagation constants and the effective indices of the two lowest order modes, respectively. p stands for polarization, which is either TE or TM. In order to have a polarization-independent device, we need to choose an appropriate cross-section geometry of the multimode region so that the beat lengths for TE and TM polarizations are fairly close to each other. Mathematically speaking, it is required that:

$$n_{0,TE} - n_{1,TE} \approx n_{0,TM} - n_{1,TM} \tag{2}$$

We use FIMMWAVE to calculate the modes supported by the cross section of the multimode region. Since the thickness of our Si_3N_4 platform is 300 nm, we vary the width w_{mul} and find that Eq. (2) is satisfied when w_{mul} = 10 µm, at which $n_{0,TE} - n_{1,TE} = 0.005068$ and $n_{0,TM} - n_{1,TM} = 0.005029$. The offset d between the two input waveguides is chosen to satisfy the "paired-interference" condition [22], so that the length of the MMI can be reduced by a factor of three and the bandwidth is significantly enlarged [23]. Finally, the length of the multi-mode region l_{mul} is varied and optimized. The physical dimensions of the designed PI-MMI as labeled in Fig. 1 is given in Table 1.

Table 1. Physical dimensions of the designed PI-MMI.

w_{mul} (µm)	l_{mul} (µm)	w (µm)	d (µm)
10	75.2	2.4	3.4

Figure 2(a) and (d) show the simulated power distributions within the designed PI-MMI of TE and TM polarizations at 1550 nm, respectively. The calculated transmission spectra in the cross and bar ports for both polarizations are plotted in Fig. 2 (b) and (e). The calculated phase differences between the cross and bar ports versus wavelength are plotted in Fig. 2 (c) and (f).

From the above simulation results, we can see that in a 30 nm bandwidth from 1535 nm to 1565 nm, the excess losses of each port are less than 0.23 dB, the imbalances between the two ports are less than 0.1 dB, and the phase errors are less than 0.0025π, regardless of the input polarization. For a larger bandwidth from 1500 nm to 1600 nm, these three parameters become 0.6 dB, 0.18 dB and 0.0062π. Therefore, the designed PI-MMI supports a large operating bandwidth.

2.2. *Design of the ABG*

From the preceding analysis of the PI-MMI, we see that the ABGs are really the core components which determine the overall performance of the PBS. Figure 3 is an example of the TE and TM transmission and reflection spectra of an ABG calculated theoretically (method discussed below). The PER for TE polarization is set by the depth of the TE stopband ("TE depth"), and the PER for TM is set by the side-lobe suppression ratio of the ABG ("TM SLSR"). The device operating bandwidth depends on the width of the TE stopband ("BW").

When designing the ABGs, the period of the grating is kept constant and only the amplitude profile is changed. First, we simulate a one-dimensional grating in MATLAB using the transfer matrix method as detailed in Ref. [24]. Here we only provide a brief outline. Each element of the grating has a 2×2 transfer matrix which takes the form shown in Eq. (3). Here a_m and b_m are the field amplitudes of the forward and backward traveling waves in the m^{th} element of the

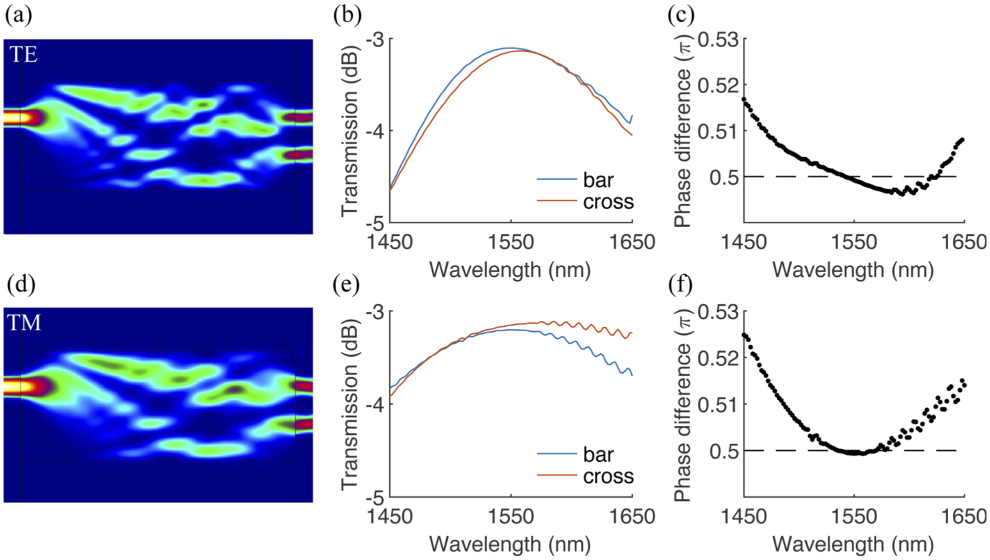

Fig. 2. (a) Simulated power distribution, (b) calculated transmissions in the bar and cross ports and (c) calculated phase difference between the cross and bar ports of TE polarization. (d) Simulated power distribution, (e) calculated transmissions in the bar and cross ports and (f) calculated phase difference between the cross and bar ports of TM polarization.

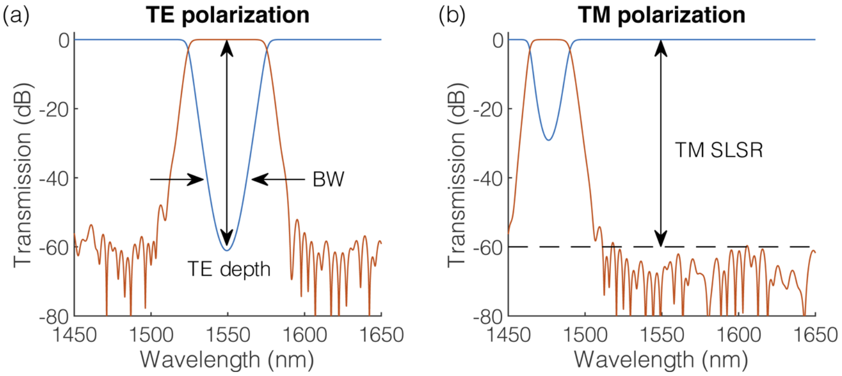

Fig. 3. Calculated spectra of an apodized grating for (a) TE and (b) TM polarizations. Blue and red curves correspond to transmission and reflection spectra, respectively.

grating, respectively.

$$\begin{bmatrix} a_{m-1} \\ b_{m-1} \end{bmatrix} = \begin{bmatrix} A_m & B_m \\ C_m & D_m \end{bmatrix} \begin{bmatrix} a_m \\ b_m \end{bmatrix} \tag{3}$$

The 2×2 matrix in Eq. (3) is the multiplication of two different types of matrices, one which describes the propagation through a homogeneous medium of a specific length and refractive index and another which describes the reflection and transmission at an interface between two adjacent sections. The expressions of A_m and B_m are given as:

$$A_m = \frac{\beta_{m-1} + \beta_m}{2\beta_m} e^{i\beta_{m-1}z}, \; B_m = -\frac{\beta_{m-1} - \beta_m}{2\beta_m} e^{-i\beta_{m-1}z} \tag{4}$$

where β_m is the propagation constant in the m^{th} element. C_m and D_m are simply the complex conjugates of B_m and A_m, respectively. Then if we multiply all matrices (total number of m) together, we will get one 2×2 matrix which describes the entire grating. This new matrix will give us the reflectance and transmittance of the device using the following relationship

$$T = \left|\frac{1}{a_0}\right|^2 = \left|\frac{1}{A}\right|^2, \; R = \left|\frac{b_0}{a_0}\right|^2 = \left|\frac{C}{A}\right|^2 \tag{5}$$

This method can be used to simulate the frequency response of an arbitrary BG. To simulate an apodized grating, we need to determine the values n_1 and n_2 which give us significant side-lobe reduction. One common method is to use a Gaussian profile such as

$$n_1(z) = n_{avg} + \Delta n \, e^{-\frac{(z-L)^2}{2\sigma^2}}, \; n_2(z) = n_{avg} - \Delta n \, e^{-\frac{(z-L)^2}{2\sigma^2}} \tag{6}$$

where $n_{avg} = (n_{max} + n_{min})/2$, $\Delta n = (n_{max} - n_{min})/2$, n_{max} and n_{min} are the effective indices of the widest and narrowest grating segments respectively, and L is the length of the grating. However, our simulations have shown better side-lobe suppression when we use a Kaiser window function as the refractive index profile, as given in Eq. (7). I_0 is the modified Bessel function of the first kind and ζ is a parameter which adjusts the shape of the curve.

$$n_1(z) = n_{avg} + \Delta n \, \frac{I_0[\zeta\sqrt{1-(2z/L)^2}]}{I_0(\zeta)} \tag{7a}$$

$$n_2(z) = n_{avg} - \Delta n \, \frac{I_0[\zeta\sqrt{1-(2z/L)^2}]}{I_0(\zeta)} \tag{7b}$$

After simulating the one-dimensional grating and finding a refractive index profile which gives significant side-lobe suppression, we need to acquire the width information of all grating segments in order to realize an actual device. To do this, we use a commercial software package (FIMMWAVE, Photon design) to simulate the cross section of our waveguide and determine a relationship between the width of the waveguide and its corresponding effective index. Based on this relationship, we then map the refractive index profile given by Eq. (7) into the actual widths of all grating segments. Last, the grating layout is generated based on this width profile.

3. Experimental results

3.1. *Fabrication and characterization methods*

The designed PBS was fabricated using the following procedures. First, 300 nm-thick Si_3N_4 was deposited by low-pressure chemical vapor deposition (LPCVD) on a Si wafer with 10 μm-thick thermal SiO_2 on top. Second, electron-beam lithography was performed (by Elionix ELS-G100) to define the pattern with a layer of ZEP-520A positive resist and a layer of AquaSAVE to prevent charge accumulation. Third, 20 nm-thick Cr was deposited as the etching mask, with which the pattern was then transferred into the Si_3N_4 layer in an inductively coupled plasma etching system. Finally, Cr mask was dissolved in acid and the upper SiO_2 cladding was deposited via plasma-enhanced chemical vapor deposition (PECVD). Figures 4(a) and (b) are two selected scanning-electron micrographs of a fabricated device.

A schematic of the experimental setup for device characterization is depicted in Fig. 4(c). Light from a tunable laser source (1450 – 1640 nm) is coupled into a polarization-maintaining (PM) fiber, which is then butt-coupled to the chip using a butt coupler [25] with a simulated coupling efficiency of $> 90\%$ for both polarizations. The input polarization is controlled by a fiber rotator. Output light from the chip is coupled to another PM fiber and then sent to a power meter for measurement. Note that an additional TE/TM filter is fabricated prior to each PBS,

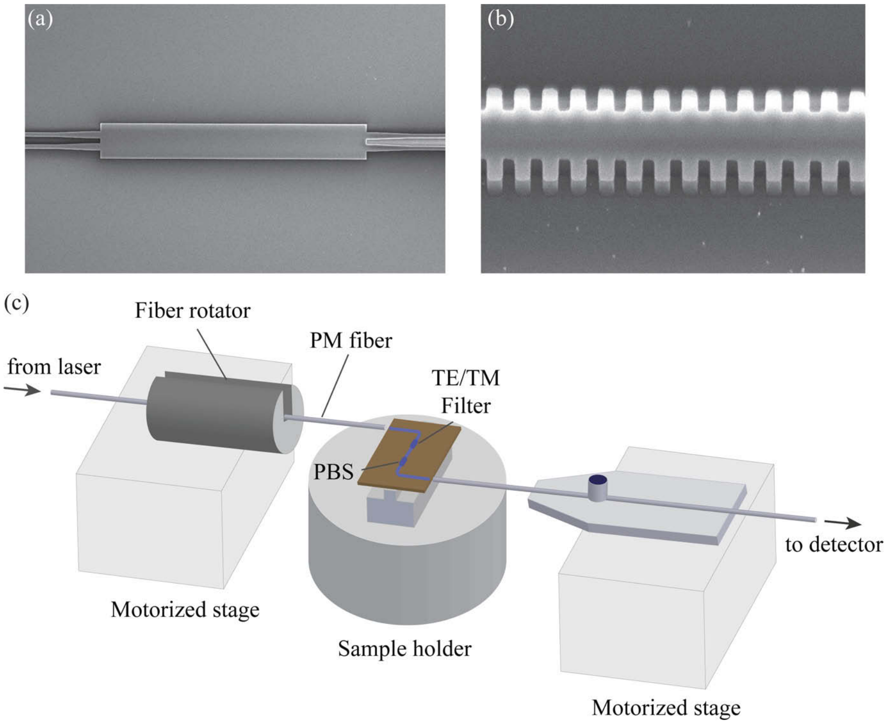

Fig. 4. Scanning-electron micrographs of (a) a PI-MMI and (b) a segment of an ABG. (c) Schematic illustration of the experimental setup.

which is able to eliminate unwanted polarization components due to the low polarization contrast of the laser source (~ 15 dB extinction ratio). For the suppression of the residual TM light, this filter is a simple bend structure as the TM bending loss is larger than that of TE. The suppression of the residual TE component is achieved by an ABG (described in Section 2.2) as a TE filter.

3.2. Experimental results: PI-MMI

The designed PI-MMI as discussed in Section 2.1 has been fabricated in a MZI configuration (as in Fig. 1, with ABGs replaced by straight waveguides) for experimental characterization. Light is injected into port 1 and we measure the power coming out from port 4 and port 2, as labeled in Fig. 1. Ideally, all light should come out of the MZI from port 4 and none from port 2. The measurement results for both polarizations are plotted in Fig. 5. The data have been normalized to a reference waveguide.

From Fig. 5, within the wavelength range 1526 nm to 1580 nm (as marked by the two vertical dotted lines), the excess loss is less than 1 dB, and the noise level at port 2 is ~ - 40 dB, for both polarizations. Comparing with the measurement results of the entire device (see the next section), we conclude that the PI-MMI itself is neither the limiting factor for the overall operating bandwidth, nor the limiting factor for the TM extinction ratio.

3.3. Experimental results: entire device

Figure 6 plots the measured transmission spectra of port 2 and 4 (as labeled in Fig. 1), together with the corresponding PERs for both polarizations. From the measurement results, we can see that a PER of > 30 dB is achieved over a bandwidth of ~ 22 nm for both polarizations. Within this

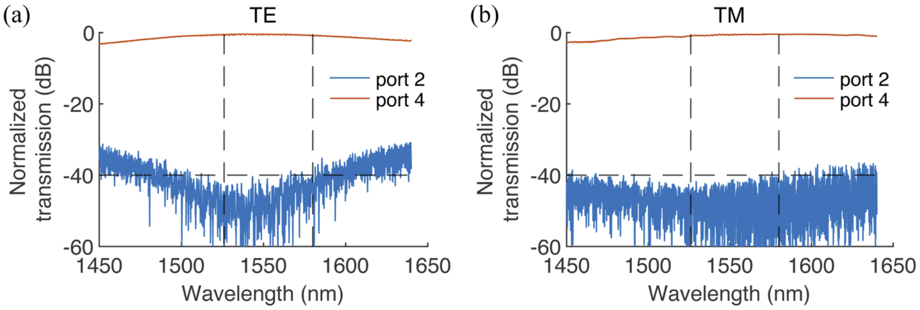

Fig. 5. Measured transmission spectra of an MZI structure made by two PI-MMIs for (a) TE and (b) TM polarizations. The blue and red curves refer to the results measured at port 2 and port 4, respectively.

bandwidth, the insertion loss is ~ 0.6 dB for TE polarization and ~ 1.1 dB for TM polarization. The measured transmission spectra have been normalized to a reference waveguide.

From Fig. 5 (b), we have already known that for TM polarization, the noise level at port 2 due to the MMI-MMI platform itself without the ABGs is roughly - 40 dB. Therefore, the - 30 dB optical power at port 2, as shown in Fig. 6(c), indicates the experimental SLSR of the ABGs that we have achieved (~ 30 dB), and it is significantly smaller than the theoretical calculation (~ 60 dB) as in Fig. 3(b), as already reported in previous works related to ABGs [26–28]. These results

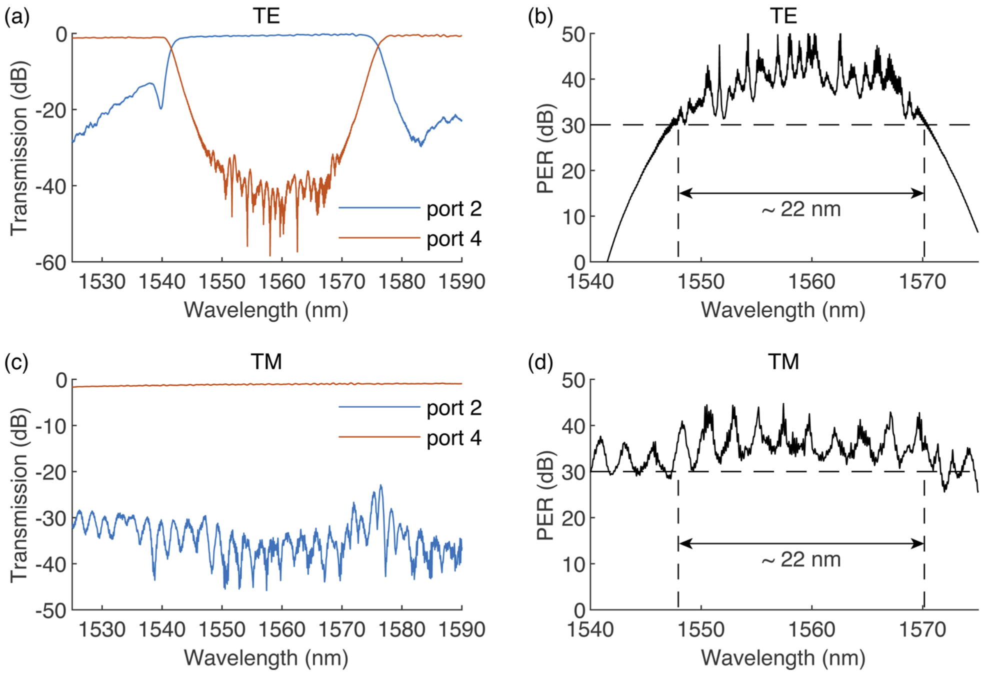

Fig. 6. (a) Measured TE spectra of port 4 (blue) and port 2 (red). (b) Extinction ratio of TE polarization, calculated by subtracting the red curve from the blue curve in (a). (c) Measured TM spectra of port 4 (blue) and port 2 (red). (d) Extinction ratio of TM polarization, calculated by subtracting the blue curve from the red curve in (c).

agree with the theoretical prediction in that the overall PER is currently limited by the TM SLSR, and the overall device bandwidth is limited by the width of the TE stopband.

4. Discussion

A comparison of the performances of several experimentally demonstrated PBSs on Si_3N_4 is given in Table 2. It can be seen that a major drawback of the PBS presented in this work is that the operating bandwidth is not large enough (~ 22 nm), which is because Bragg gratings are employed in the design for separating TE and TM polarizations. It is possible to increase the bandwidth slightly by implementing ABGs with a larger index step, however, it is very difficult to acquire a large bandwidth (e.g., > 60 nm) while maintaining similar insertion loss by simply implementing stronger gratings, because of the extra loss induced by the backward cladding-mode coupling in integrated Bragg gratings [29].

Table 2. Comparison of several experimentally demonstrated Si_3N_4-based PBSs.

Structure	PER (dB)	IL (dB)	BW (nm)	Length (µm)	Ref.
MZI	> 20	< 0.4	35	113	[20]
DC-MZI w/ active control	> 20 37	1	39 at 1554	1000	[21]
phase-controlled DC	> 20	< 1.3	95	136	[30]
3D DC	> 16	1	30	800	[31]
angled MMI	> 18	0.8	100	80	[19]
cascaded DC	> 10	~ 2	80	112	[32]
PI-MMI + ABG	> 30	~ 1.1	22	820	This work

From Table 2, we also see that many current PBS designs involve directional couplers. As the performance of a DC is sensitive to the variation of the gap width due to fabrication imperfections, one advantage of our design based on PI-MMI and ABG is the device robustness. The experimental results demonstrated in Fig. 6 are easy to reproduce, as there was no time-consuming tuning of design parameters needed.

In order to improve the TM SLSR for a larger overall PER, a further investigation of the ABGs is needed. When we simulated the reflection spectrum of an ABG with its both ends truncated (i.e., replace the sections in which the width variations are less than 20 nm with simple straight waveguides), we saw a drastic decrease of the SLSR to ~ 30 dB. Therefore, we believe that the degradation of the SLSR is, at least partially, due to the inaccuracy of electron-beam lithography at both ends of the grating structure, where the width corrugations are less than ~ 20 nm. Possible solutions to "amplify" the width variations include: (1) introducing a phase difference between the two sidewalls of the grating [28], and (2) putting grating structures away from the center waveguide (i.e., cladding modulation) [33].

Depending on the application, one needs to choose from different PBS designs. For example, in order to realize polarization-independent astrophotonic devices, it is more important to have a large bandwidth than to have a large PER. In this case, a PBS design based on directional couplers or angled MMIs is preferred. However, for some quantum photonic applications in which light is emitted by ions, it is not quite necessary to have a large bandwidth since the linewidth of the ion emission is quite narrow. In this case, the higher the PER, the better the device. We believe that our PBS design which exhibits a stable PER of > 30 dB is suitable for these quantum photonic applications.

5. Conclusion

In this work, we have presented the design, fabrication and characterization of a novel polarization beam splitter on a Si_3N_4 platform. An extinction ratio of > 30 dB is achieved over a 22 nm bandwidth for both polarizations, with an insertion loss of ~ 1.1 dB. Possible approaches for further improvements are discussed. As photonic quantum technologies are rapidly evolving, we believe that integrated polarization beam splitters will play a critical role in the anticipated future.

Funding. National Aeronautics and Space Administration (16-APRA16-0064).

Disclosures. The authors declare no conflicts of interest.

References

1. J. B. Hawthorn and P. Kern, "Astrophotonics: a new era for astronomical instruments," Opt. Express **17**(3), 1880–1884 (2009).
2. P. Gatkine, S. Veilleux, and M. Dagenais, "Astrophotonic spectrographs," Appl. Sci. **9**(2), 290 (2019).
3. T. Zhu, Y. Hu, P. Gatkine, S. Veilleux, J. Bland-Hawthorn, and M. Dagenais, "Arbitrary on-chip optical filter using complex waveguide Bragg gratings," Appl. Phys. Lett. **108**(10), 101104 (2016).
4. Y. W. Hu, S. Xie, J. Zhan, Y. Zhang, S. Veilleux, and M. Dagenais, "Integrated arbitrary filter with spiral gratings: Design and characterization," J. Lightwave Technol. **38**(16), 4454–4461 (2020).
5. H. Terashima, S. Kobayashi, T. Tsubakiyama, and K. Sanaka, "Quantum interferometric generation of polarization entangled photons," Sci. Rep. **8**(1), 15733 (2018).
6. M. Rezai, J. Wrachtrup, and I. Gerhardt, "Polarization-entangled photon pairs from a single molecule," Optica **6**(1), 34–40 (2019).
7. T. Rudolph, "Why I am optimistic about the silicon-photonic route to quantum computing," APL Photonics **2**(3), 030901 (2017).
8. J. L. O'Brien, A. Furusawa, and J. Vučković, "Photonic quantum technologies," Nat. Photonics **3**(12), 687–695 (2009).
9. D. Dai and J. E. Bowers, "Novel ultra-short and ultra-broadband polarization beam splitter based on a bent directional coupler," Opt. Express **19**(19), 18614–18620 (2011).
10. H. Wu, Y. Tan, and D. Dai, "Ultra-broadband high-performance polarizing beam splitter on silicon," Opt. Express **25**(6), 6069–6075 (2017).
11. Y. Tian, J. Qiu, C. Liu, S. Tian, Z. Huang, and J. Wu, "Compact polarization beam splitter with a high extinction ratio over S + C + L band," Opt. Express **27**(2), 999–1009 (2019).
12. J. R. Ong, T. Y. L. Ang, E. Sahin, B. Pawlina, G. F. R. Chen, D. T. H. Tan, S. T. Lim, and C. E. Png, "Broadband silicon polarization beam splitter with a high extinction ratio using a triple-bent-waveguide directional coupler," Opt. Lett. **42**(21), 4450–4453 (2017).
13. Y. Kim, M. H. Lee, Y. Kim, and K. H. Kim, "High-extinction-ratio directional-coupler-type polarization beam splitter with a bridged silicon wire waveguide," Opt. Lett. **43**(14), 3241–3244 (2018).
14. S. Lin, J. Hu, and K. B. Crozier, "Ultracompact, broadband slot waveguide polarization splitter," Appl. Phys. Lett. **98**(15), 151101 (2011).
15. L. Xu, Y. Wang, A. Kumar, D. Patel, E. El-Fiky, Z. Xing, R. Li, and D. V. Plant, "Polarization beam splitter based on MMI coupler with SWG birefringence engineering on SOI," IEEE Photonics Technol. Lett. **30**(4), 403–406 (2018).
16. X. Sun, J. S. Aitchison, and M. Mojahedi, "Realization of an ultra-compact polarization beam splitter using asymmetric mmi based on silicon nitride / silicon-on-insulator platform," Opt. Express **25**(7), 8296–8305 (2017).
17. Y. Huang, Z. Tu, H. Yi, Y. Li, X. Wang, and W. Hu, "High extinction ratio polarization beam splitter with multimode interference coupler on SOI," Opt. Commun. **307**, 46–49 (2013).
18. S. Hassan, D. Chack, and V. Mahajan, "High extinction ratio and low loss polarization beam splitter based on multimode interference for PICs," Appl. Opt. **59**(11), 3369–3375 (2020).
19. R. Kudalippalliyalil, T. E. Murphy, and K. E. Grutter, "Low-loss and ultra-broadband silicon nitride angled mmi polarization splitter/combiner," Opt. Express **28**(23), 34111–34122 (2020).
20. S. Gao, Y. Wang, K. Wang, and E. Skafidas, "Low-loss and broadband 2 × 2 polarization beam splitter based on silicon nitride platform," IEEE Photonics Technol. Lett. **28**(18), 1936–1939 (2016).
21. J. Feng and R. Akimoto, "Silicon nitride polarizing beam splitter with potential application for intersubband-transition-based all-optical gate device," Jpn. J. Appl. Phys. **54**(4S), 04DG08 (2015).
22. L. B. Soldano and E. C. M. Pennings, "Optical multi-mode interference devices based on self-imaging: principles and applications," J. Lightwave Technol. **13**(4), 615–627 (1995).
23. S. Xie, J. Zhan, Y. Hu, Y. Zhang, S. Veilleux, J. Bland-Hawthorn, and M. Dagenais, "Add–drop filter with complex waveguide Bragg grating and multimode interferometer operating on arbitrarily spaced channels," Opt. Lett. **43**(24), 6045–6048 (2018).
24. A. Yariv and P. Yeh, *Photonics: Optical Electronics in Modern Communications* (Oxford University, 2006).
25. T. Zhu, Y. Hu, P. Gatkine, S. Veilleux, J. Bland-Hawthorn, and M. Dagenais, "Ultrabroadband high coupling efficiency fiber-to-waveguide coupler using si $_3n_4$ /sio$_2$ waveguides on silicon," IEEE Photonics J. **8**(6), 1–7 (2016).

26. A. D. Simard, N. Belhadj, Y. Painchaud, and S. LaRochelle, “Apodized silicon-on-insulator Bragg gratings,” IEEE Photonics Technol. Lett. **24**(12), 1033–1035 (2012).
27. A. D. Simard, Y. Painchaud, and S. LaRochelle, “Integrated Bragg gratings in spiral waveguides,” Opt. Express **21**(7), 8953–8963 (2013).
28. R. Cheng, H. Yun, S. Lin, Y. Han, and L. Chrostowski, “Apodization profile amplification of silicon integrated Bragg gratings through lateral phase delays,” Opt. Lett. **44**(2), 435–438 (2019).
29. J. Zhan, Y. Zhang, Y. Hu, S. Xie, S. Veilleux, and M. Dagenais, “Investigation of backward cladding-mode coupling in bragg gratings implemented on a si3n4 waveguide platform,” J. Opt. Soc. Am. B **36**(12), 3442–3449 (2019).
30. S. Guerber, C. Alonso-Ramos, D. Benedikovic, E. Durán-Valdeiglesias, X. Le Roux, N. Vulliet, E. Cassan, D. Marris-Morini, C. Baudot, F. Boeuf, and L. Vivien, “Broadband polarization beam splitter on a silicon nitride platform for O-band operation,” IEEE Photonics Technol. Lett. **30**(19), 1679–1682 (2018).
31. J. Feng and R. Akimoto, “A three-dimensional silicon nitride polarizing beam splitter,” IEEE Photonics Technol. Lett. **26**(7), 706–709 (2014).
32. B. Bhandari, C.-S. Im, O. R. Sapkota, and S.-S. Lee, “Highly efficient broadband silicon nitride polarization beam splitter incorporating serially cascaded asymmetric directional couplers,” Opt. Lett. **45**(21), 5974–5977 (2020).
33. D. T. H. Tan, K. Ikeda, and Y. Fainman, “Cladding-modulated Bragg gratings in silicon waveguides,” Opt. Lett. **34**(9), 1357–1359 (2009).